

Multiple low-energy excitons and optical response of d^0 double perovskite $\text{Ba}_2\text{ScTaO}_6$

A. K. Himanshu,^{1,2,*} Sujit Kumar,³ Urmimala Dey,^{4,5} and Rajyavardhan Ray^{6,7,8,†}

¹*Variable Energy Cyclotron Center (VECC), DAE, 1/AF Bidhannagar, Kolkata, India 700064*

²*Homi Bhabha National Institute, Mumbai, India 400094*

³*Department of Physics, Magadh University, Bodh Gaya, India 824234*

⁴*Department of Physics, Indian Institute of Technology Kharagpur, Kharagpur, India 721302*

⁵*Department of Physics, Durham University, South Road, Durham DH1 3LE, UK*

⁶*Leibniz IFW Dresden, Helmholtzstr. 20, 01069 Dresden, Germany*

⁷*Dresden Center for Computational Materials Science (DCMS), TU Dresden, D-01062, Germany*

⁸*Department of Physics, Birla Institute of Technology Mesra, Ranchi, India 835215*

(Dated: April 14, 2022)

Large bandgap insulators are considered promising for applications such as photocatalysts, dielectric resonators and interference filters. Based on synchrotron X-ray diffraction, diffuse reflectance measurement and density functional theory, we report the crystal structure, optical response, and electronic properties of the synthesized d^0 double perovskite $\text{Ba}_2\text{ScTaO}_6$. In contrast to earlier prediction, the electronic bandgap is found to be large, ~ 4.66 eV. The optical response is characterized by the presence of multiple exciton modes extending up to the visible range. A detailed investigation of the direct gap excitons based on the Elliot formula is presented. Density functional theory based investigation of the electronic properties within generalized gradient approximation severely underestimates the electronic gap. To reach a quantitative agreement, we consider different available flavors of the modified-Becke-Johnson exchange-correlation potential and discuss their effects on the electronic and optical properties.

PACS numbers: 61.10.Nz, 78.20.-e, 71.15.Mb, 78.40.-q

Keywords: Double Perovskites, SXRD, UV-Vis spectroscopy, Excitons, mBJ, DFT

I. INTRODUCTION

Double Perovskite oxides (DPOs), with the general formula $\text{A}_2\text{BB}'\text{O}_6$, constitute an important materials class exhibiting a wide variety of interesting physical phenomena, like high temperature superconductivity, colossal magnetoresistance, photocatalytic activity, high dielectric constants, etc. [1–7]. In ordered systems, the transition-metals B and B' are surrounded by oxygen atoms in an octahedral environment with B–O–B' links. Therefore, DPOs consist of alternating corner sharing BO_6 and $\text{B}'\text{O}_6$ octahedra stacked in all three directions. On the other hand, the A-sites, centered at the interstitial voids created by these octahedra, are typically occupied by divalent alkaline earth metals or trivalent rare-earth metals. Depending on relative size of the cations to anions, different structures may be realized: ideally, DPOs have a cubic structure and is realized in most cases at high temperatures. However, depending on the size, A-site cations may induce tilting and rotations of the BO_6 and $\text{B}'\text{O}_6$ octahedra, leading to deviations from the ideal cubic structure. The resulting low-symmetry structure could be tetragonal, monoclinic, orthorhombic, or rhombohedral. A schematic representation of an ordered cubic DPO is shown in Fig. 1(b). The presence of different metal sites (A-, B- and B'-sites) allows a high degree of flexibility in crystal structure, opto-electronic and magnetic properties, responsible for the mentioned range of interesting phenomena. This further makes them appealing for novel device applications.

The large-gap d^0 -DPOs formed by transition metals with unfilled/empty valence d -shells are of special interest [5–7]. They are considered promising in microwave-dielectric resonator applications, including interference filters, reflective coating and in optical fibers, due to their good dielectric properties, and as buffer materials due to their low reactivity. The properties of such materials are largely governed by the transition metal species and structural distortions [5, 6]. For example, it was found that the bandgap increases with increasing octahedral tilting and distortions. Moreover, difference in the electronegativity of the B and B' cations can significantly affect the electronic bandgaps: compositional modulations can alter the bandgap by up to 2 eV [5]. Therefore, to ascertain the feasibility

* akhimanshu@gmail.com

† r.ray@bitmesra.ac.in

of these materials for possible technological applications, a detailed characterization of their optical response over a wide frequency range is indispensable.

In this combined experimental and theoretical study, we focus on $\text{Ba}_2\text{ScTaO}_6$. Among the Ta-based DPOs, $A_2\text{MTaO}_6$, $M = \text{Sc}$ compounds are slightly different from other members of the family in terms of their bandgap [5]. Further, the electronic bandgap of $\text{Ba}_2\text{ScTaO}_6$ was predicted to be the smallest (3.35 eV) within the $A_2\text{ScTaO}_6$ compounds. With decreasing size of A cations, octahedral rotations and distortions induce a larger bandgap. The formal valencies of Sc and Ta are, respectively, +3 and +5, leading to the d^0 configuration for both the involved transition metals. The ionic radii of the transition metal cations are found to be 0.745 Å and 0.64 Å for Sc^{3+} and Ta^{5+} , respectively. Large difference in the ionic radii is expected to lead to a long-range ordering of the BO_6 and $\text{B}'\text{O}_6$ octahedra in the crystal structure. A good measure of the crystal structure symmetry of perovskite oxides is the tolerance factor [3–6, 8, 9]. For $\text{Ba}_2\text{ScTaO}_6$, the tolerance factor is found to be $t = 1.02$ [5], implying the likelihood of a cubic symmetry since $t \approx 1$.

The primary objective of this study was to ascertain the origin of low predicted bandgap of $\text{Ba}_2\text{ScTaO}_6$: whether this is an intrinsic property of the material or arises due to DFT approximations. To this end, we report the crystal structure, obtained via synchrotron X-ray diffraction (SXRD), and the optical gap, obtained via the diffuse reflectance measurement in the UV-Vis range. We find that $\text{Ba}_2\text{ScTaO}_6$ crystallizes in an ordered cubic structure and has a gap of ~ 4.7 eV, similar to other $A_2\text{MTaO}_6$ ($M = \text{Y}$, Al and Ga). For the synthesized DPO $\text{Ba}_2\text{ScTaO}_6$, we have performed a thorough investigation of the electronic and optical properties within the framework of density functional theory (DFT). Standard DFT using generalized gradient approximation (GGA) agrees with the earlier reports. A quantitative agreement between theory and experiments is, however, found only upon including the modified Becke-Johnson (mBJ) exchange-correlation potential. This leads to accurate predictions of the optical response, especially beyond the experimental range. Inclusion of the mBJ potential reduces the conduction bandwidth of the t_{2g} states and increases the bandgap. In particular, our comparative study of different parametrizations of the mBJ potential clarifies the most suitable choice of mBJ potential for $\text{Ba}_2\text{ScTaO}_6$ and likely also for other materials with similar bandgap and electronic properties.

II. EXPERIMENTAL AND COMPUTATIONAL DETAILS

A. Synthesis and characterization

$\text{Ba}_2\text{ScTaO}_6$ was synthesized by conventional solid state reaction at 1500 °C for 72 hours, from a mixture of BaCO_3 (99%, Merc India), Sc_2O_3 (99.99%, Alfa Aesar), Ta_2O_5 (99.99%, Aldrich) powders in stoichiometry proportions. Color of the obtained samples was found to be off-white. Synchrotron X-ray Diffraction (SXRD) study was carried out using BL-11 of Indus-2 synchrotron source [10], using $\lambda = 0.46195$ Å beam with a beam current of 100 meV and energy 2.5 GeV, at the Raja Ramanna Center for Advanced Technology (RRCAT), Indore, India. The Rietveld analysis software FULLPROF [11] was used to analyze the SXRD data, which shows a cubic structure, space group $Fm\bar{3}m$ (No. 225). Ba, Sc, Ta, and O atoms occupy the Wyckoff positions of 8c, 4a, 4b and 24e, respectively. The SXRD pattern and the Rietveld fit are shown in Fig. 1(a). The crystal structure is shown in Fig. 1(b) and the corresponding details related to the structural and the refinement parameters are listed in Table I.

B. UV-Vis spectroscopy

Diffusive reflectance spectroscopy was carried out in the UV-Vis range using the UV-Vis spectrophotometer Perkin-Elmer 950. In order to estimate the electronic gap, the measured reflectance spectrum was converted into an effective absorption spectrum — the Kubelka-Munk (KM) function, $F(R)$ [12, 13]. Within this approach, the electronic bandgap is obtained using [6]:

$$F(R) \propto \frac{(\hbar\omega - E_g)^n}{\hbar\omega}, \quad (1)$$

with $n = 1/2$ corresponds to direct-allowed transitions. $\hbar\omega$ and E_g are the incident photon energy and the gap, respectively. As outlined in [6], the intercept of the linear part of $[F(R)\hbar\omega]^2$ vs $\hbar\omega$ curve on the energy axis is the bandgap. Figure 1(c) shows the absorption spectrum (KM function) and the corresponding value of optical gap. The value of the bandgap was found to be 4.57 eV.

However, a closer look at the absorption spectrum (KM function, $F(R)$) in the log-scale reveals multiple low-intensity peaks in the energy range between 1.4 eV and 4.2 eV, shown in Fig. 2(a). These peaks indicate presence of

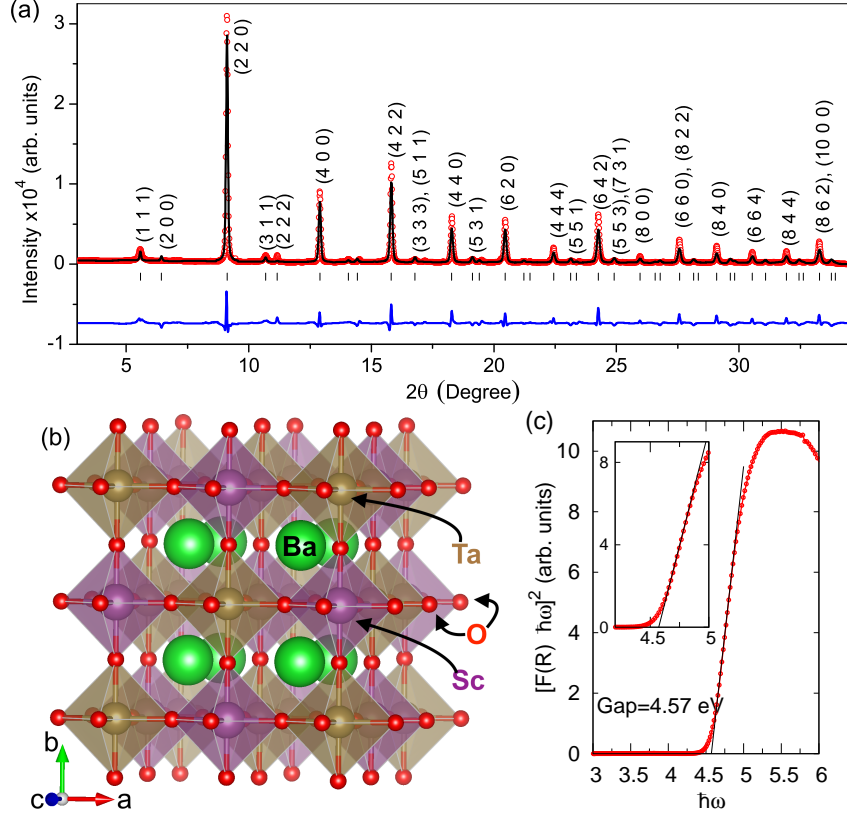


FIG. 1: (Color online.) (a) The SXRD pattern and (b) the crystal structure of $\text{Ba}_2\text{ScTaO}_6$. The corresponding crystal structure parameters are provided in Table I. (c) The dependence of the modified Kubelka-Munk (KM) function, corresponding to direct-allowed transitions, on the photon energy $\hbar\omega$ and the linear part showing an optical band-gap of 4.57 eV. The inset shows a zoom of the plot near the gap energy.

exciton modes. To obtain details regarding these exciton modes, the absorption data was modeled based on the Elliot formula for direct-gap excitons [14, 15]. The absorption is thus given by a combination of excitonic contributions, α_{nx} , and a continuum, α_{cont} , contributing at low (band edge) and high energies, respectively [15]:

$$\begin{aligned}
 \alpha(\omega) &= \sum_n \alpha_{nx}(\omega) + \alpha_{\text{cont}}(\omega) \\
 &= \sqrt{E_b} \left[\sum_n 2A_n \frac{E_b}{n^3} \text{sech} \left(\frac{\hbar\omega - E_g + E_b/n^2}{\Gamma_n} \right) \right. \\
 &\quad \left. + B \int_{E_g}^{\infty} \text{sech} \left(\frac{\hbar\omega - E}{\Gamma'} \right) \right. \\
 &\quad \left. \times \frac{1 + 10 \frac{m^2}{\hbar^4} EC_{np} + \left(\frac{\sqrt{126}m^2}{\hbar^4} EC_{np} \right)^2}{1 - \exp \left(-2\pi \sqrt{\frac{E_b}{E - E_g}} \right)} dE \right]. \quad (2)
 \end{aligned}$$

Here, n stands for the order of the exciton state. α_{nx} , therefore, corresponds to the absorption from the n -th exciton state. ‘sech’ function is used as a broadening function for the exciton lineshape with a linewidth Γ_n . E_g is the electronic bandgap while E_b is the exciton binding energy. C_{np} is the correction factor to account for deviations from parabolic bands. B and Γ' , respectively, denote the amplitude and the broadening for the continuum part. m is the free electron mass and \hbar is the reduced Planck constant.

A least-squares fit of the above expression in Eq. (2) to the data was obtained using the python-lmfit function and scipy (python version 3.8.12). For brevity, the low-energy part, up to 4.2 eV, consisting of multiple exciton peaks (marked by arrows in Fig. 2(a)) and the high energy part were considered separately. For the high energy part, above

photon energy $\hbar\omega = 5.2$ eV, deviations between the calculated and the observed spectrum were noted for all cases discussed below. Therefore, only fitting up to 5.2 eV was considered.

Different models were considered for the high-energy part of the absorption data: first, given the exponential onset of the absorption spectrum in this energy window, thus describing the data by a Urbach tail [$U(\omega) = U_0 \exp\{(\omega - E_U)/E_U\}$; E_U is the Urbach energy while E_1 and U_0 are fitting parameters] and a direct gap function [Eq. (1)], as shown in Fig. 2(b). Second, a fit of $\alpha(\omega)$ consisting of one exciton mode (with a suitable value of $n = 7$) was also investigated. For the latter, the best-fit was obtained for $E_g = 4.66$ eV ($\chi^2 = 1.181 \times 10^{-3}$) and is shown in Fig. 2(c).

On the other hand, for the low-energy part of the data, a fit of $\alpha'(\omega) = \sum_n \alpha_{nx}$ was successfully obtained with six exciton mode peaks. Furthermore, it should be noted that the data around the first peak, at ~ 1.76 eV, is asymmetric. Therefore, to reliably obtain the value of the peak position, an “offset” to the sech function, leading to $\beta(\omega) = \sum_n \alpha_{nx} + k_n$, was also considered. However, the resulting values of offsets were found to be negative. Alternatively, we considered a hypothetical peak at the edge of the data to account for the offset in only the first peak. This immediately led to a remarkable fit to the data and is shown in Fig. 2(d). The reliability of the estimation of the this peak position was tested by considering an isolated fit of the $\alpha'(\omega)$ with a constant offset.

The resulting best-fit ($\chi^2 = 7.41 \times 10^{-5}$) corresponds to $E_g = 4.66$ eV. However, the quality of the fit remained unchanged for small changes in the values of E_g . For example, with $E_g = 4.67, 4.68$ eV, the difference in χ^2 from the fit with $E_g = 4.66$ is $\Delta\chi^2 \sim 10^{-10}$.

Other models, such as a five exciton peak model and four exciton peak models were also considered but led to a poorer fit ($\chi^2_{5\text{-peak}} = 7.570 \times 10^{-5}$; $\chi^2_{4\text{-peak}} = 8.196 \times 10^{-5}$). In the following, we will, therefore, consider the electronic gap of $\text{Ba}_2\text{ScTaO}_6$ to be $E_g = 4.66$ eV.

C. Density functional theory

We adopted the all electron full-potential linearized augmented plane wave (FP-LAPW) method of DFT with the scalar relativistic approximation, as implemented in the WIEN2k code [16, 17]. All calculations were carried out for the experimental crystal structure (Table I), using a $12 \times 12 \times 12$ k -mesh in the full Brillouin zone (BZ) (~ 72

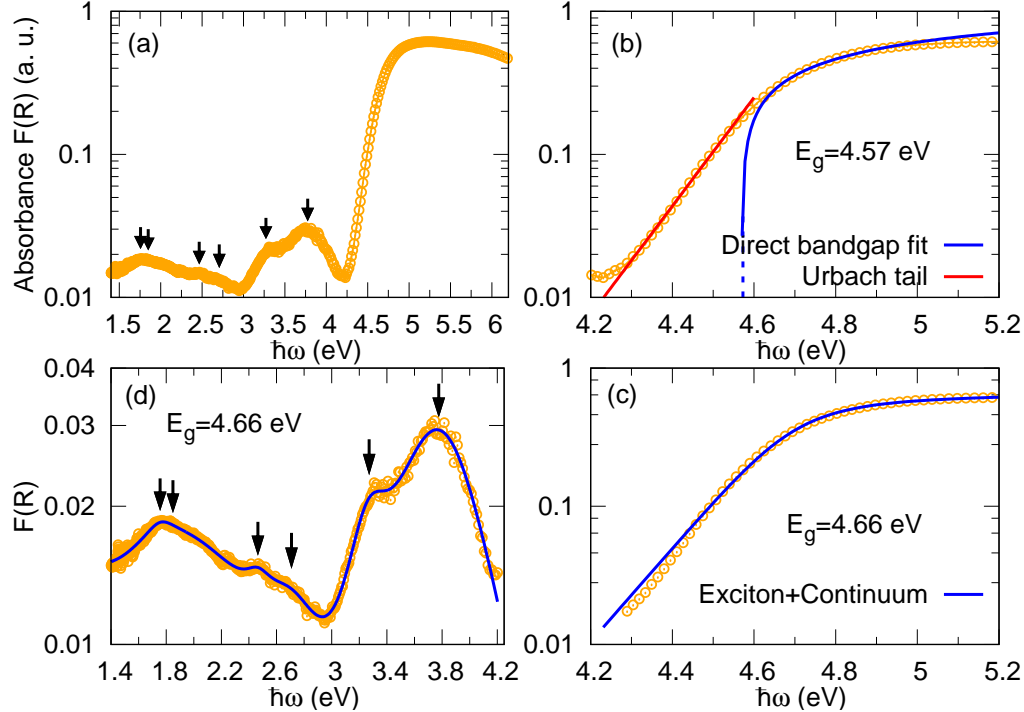


FIG. 2: (Color online.) (a) The absorption spectrum of $\text{Ba}_2\text{ScTaO}_6$. The arrows indicate the exciton modes. (b)-(c) Fit of the high-energy part of the absorption spectrum to (b) direct-allowed optical transition with Urbach tail, (c) continuum model with and without exciton modes. (d) The low-energy part of the absorption spectrum (symbols) and a fit of the 6-peak exciton model (solid line).

k -points in the irreducible Brillouin zone) to carry out the integrals over the BZ. The muffin-tin radii for Ba, Sc, Ta, and O were kept fixed at 2.5 a.u., 2.3 a.u., 2.03 a.u. and 1.54 a.u., respectively. The $R_{MT} \times k_{\max}$ parameter was chosen to be 7.0, where k_{\max} is the plane-wave cut-off and R_{MT} is the smallest muffin-tin radii among all atoms. The exchange and correlation effects have been treated within the Perdew-Burke-Erzenhof (PBE) implementation of the Generalized Gradient Approximation (GGA) [18]. Self-consistent solutions correspond to convergence below 0.0001 e/a.u.³ for charge, and 0.01 mRy for the total energy per unit cell.

In order to address the well-known issue of bandgap underestimation within DFT [19], calculations were also performed using the semi-local Tran-Blaha modified Becke-Johnson (TB-mBJ) exchange-correlation potential [20], as implemented in WIEN2k. Different implementations of the mBJ potential available in WIEN2k were also tested: in particular, the refined mBJ potentials suitable for perovskite oxides [21], large bandgap solids [21] and halide perovskites [22].

The optical properties were obtained using complex dielectric function

$$\varepsilon(\omega) = \varepsilon_1(\omega) + i\varepsilon_2(\omega). \quad (3)$$

In general, ε is a second rank tensor with nine independent components. However, depending on the crystalline symmetry, only a few of these components could be independent. For a cubic structure, for example, the three principal directions (x , y , and z) are equivalent, leading to only one independent value. The real and imaginary part of the dielectric response function are related by Kramers-Kronig relation:

$$\varepsilon_{1,ij}(\omega) = \delta_{ij} + \frac{2}{\pi} \mathcal{P} \int_0^\infty \frac{\omega' \varepsilon_{2,ij}(\omega')}{\omega'^2 - \omega^2} d\omega' \quad (4)$$

where, \mathcal{P} stands for the principal part of the integral and $\varepsilon_{a,ij}$ is the ij -th component of ε_a ($a = 1, 2$). All other optical response functions, such as the refractive index, optical conductivity, absorption coefficient and the electron loss function, were obtained by using their well-defined mathematical relations with the dielectric function [23]. The broadening parameter was chosen to be 0.1 eV.

III. RESULTS AND DISCUSSIONS

A. Crystal structure

Ba₂ScTaO₆ crystallizes in a cubic $Fm\bar{3}m$ structure (No. 225) with lattice constant $a = 8.226$ Å. The only free parameter in this structural model, *viz.* the x -coordinate for the O atom is found to be $x = 0.245$ based on a high-resolution SXRD data. The complete details of the crystal structure are listed in Table I. Within the cubic symmetry, the Sc-O-Ta angle is 180°. The M-O bond lengths are 2.0894 Å and 2.0236 Å, for M= Sc and Ta, respectively. These values are in excellent agreement with the earlier reported X-ray diffraction data in the Springer Materials database [24, 25], but deviate slightly from the prediction based on SPuDS [26].

B. Exciton modes, optical and electronic gaps

UV-Vis spectroscopy is a convenient way of obtaining the electronic/optical gap of a semiconductor. The simplest way to estimate the electronic bandgap is through the KM function [Eq. (1)]. Figure 1(c) shows the modified KM function corresponding to direct-allowed transitions (see Sec. II B) as a function of the incident photon energy. The bandgap is obtained by taking the intercept of the low-energy linear part of this curve on the energy axis [6, 12, 13], which is estimated to be 4.57 eV.

In general, however, the electronic bandgap, defined as the energy difference between the valence band maxima and the conduction band minima, can turn out to be significantly different from the optical gap due to presence of exciton modes, $d-d$ transitions, phonon absorption and emission, etc. [27, 28]. In such cases, the above analysis breaks down rendering the estimate of the electronic gap inaccurate.

The absorption spectrum (KM function) of Ba₂ScTaO₆ in log-scale, shown in Fig. 2(a), reveals that the low-energy part up to ~ 4.2 eV contains multiple low-intensity peaks corresponding to exciton modes, marked by arrows. A high quality fit of $\alpha_{nx}(\omega)$ [Eq. (2)] can be obtained with six exciton peaks ($n = 1 \dots 6$), at approximately 1.76 eV, 1.85 eV, 2.47 eV, 2.71 eV, 3.27 eV and 3.78 eV. Correspondingly, the renormalized exciton binding energies, E_b/n^2 , are 2.904 eV, 2.81 eV, 2.20 eV, 1.95 eV, 1.39 eV and 0.88 eV, respectively. The electronic bandgap E_g is found to be 4.66 eV, and the resulting fit is shown in Fig. 2(d).

TABLE I: Crystal structure and refinement parameters for Ba₂ScTaO₆ obtained from SXRD data at room temperature. The atomic positions are in fractions coordinates (x,y,z) along with their Wyckoff positions (WPs).

A. Refinement parameters					
Params.		Value			
Space group		$Fm\bar{3}m$ (No. 225)			
$a = b = c$ (Å)		8.226			
$\alpha = \beta = \gamma$		90°			
Vol (Å ³)		556.5(4)			
Formula units/unit cell		$Z = 4$			
Final R -indices:					
R_p		4.17%			
R_{wp}		3.79%			
R_{exp}		2.81%			
χ^2		2.35			
B. Structural parameters					
Atoms	WP	x	y	z	B (Å)
Ba	8c	1/4	1/4	1/4	0.12(2)
Sc	4b	1/2	1/2	1/2	0.11(1)
Ta	4a	0	0	0	0.23(1)
O	24e	0.245(3)	0	0	0.08(0)

The high-energy part, corresponding to photon energies above 4.2 eV is characteristically defined by a continuum absorption spectrum. To model this part of the spectrum, different models were considered: first, driven by the exponential tail of the absorption data in this energy window, we considered the simplistic view based on direct-allowed transitions without excitons. The band edge part of the data is modeled as an exponential tail, so called Urbach tail, usually ascribed to shallow traps and disorder [29, 30]. The Urbach energy was obtained to be 114.42 meV from our room temperature data. The corresponding fit is shown in Fig. 2(b). While it is apparent that the data can be described reasonably well, the estimated gap is at odds with the estimated (electronic) bandgap $E_g = 4.66$ eV obtained from the low-energy part. Moreover, due to the presence of the excitons, the continuum absorption spectrum is also affected [14, 15] which is not accounted for in this model.

Later, the full expression for $\alpha(\omega)$ given in Eq. (2) was considered with one (possible) exciton mode ($n = 7$) and $E_g = 4.66$ eV. The best-fit, shown in Fig. 2(c), corresponds to $\frac{m^2}{\hbar^4} C_{np} = -0.003$ eV⁻¹, showing that there is no significant deviation from parabolic bands. The exciton binding energy was found to be 0.11 eV. Small deviations are, however, observed in the energy window between 4.2 eV and 4.5 eV. We, therefore, conclude that the electronic gap of Ba₂ScTaO₆ is 4.66 eV while the optical gap is smaller ~ 1.4 eV.

The presence of exciton modes in the visible range (1.75 eV to 3.1 eV) has an important consequence: based on the estimated gap of 4.66 eV, Ba₂ScTaO₆ samples should be white in color due to lack of absorption in the visible range. However, even if of low intensity, presence of the exciton modes in the green (~ 2.3 eV) and red (~ 1.8 eV) regions, implies small absorption leading to the off-white color.

C. Electronic structure

DFT calculations using GGA lead to a non-magnetic insulating ground state for Ba₂ScTaO₆. The corresponding total and partial densities of states (DOS) are shown in Figure 3(a), clearly exhibiting the insulating nature. The electronic properties of insulator DPOs can be well-described by the crystal field experienced by the M- d states and hybridization between the oxygen 2p states and the M- d states. The crystal field produced by the nearest oxygen atoms in an octahedral geometry lifts the five-fold degeneracy of M- d states and leads to splitting into the lower lying t_{2g} states, consisting of d_{xy} , d_{yz} , d_{xz} orbitals, and e_g states, consisting of $d_{x^2-y^2}$ and d_{z^2} orbitals. Typical of DPOs, hybridization with the surrounding oxygen atoms leads to bonding states with dominant contribution from the O- p orbitals in valence band while the conduction band edge comprises of anti-bonding states with dominant d contribution. The relative energy position of the transition metal d states, however, depends on the metal species (electronegativity, ionic radii, etc.) and occupation of the d shell.

Indeed, for Ba₂ScTaO₆, where both the transition metals are formally unoccupied (d^0 -ness), the M- d states (both t_{2g} and e_g states) for M = Sc as well as M = Ta lie in the conduction band, as shown in Fig. 3(a). This, in turn, confirms the formal valencies of +3 and +5 for Sc and Ta, respectively.

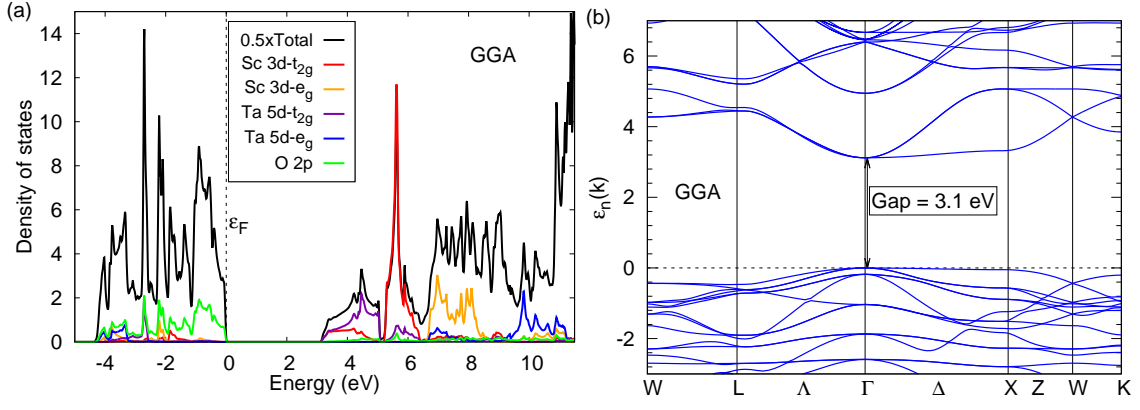


FIG. 3: (Color online.) (a) The total and partial densities of states in states/eV-unit cell and states/eV-atom, respectively, obtained within GGA. The corresponding bandstructure showing the direct gap.

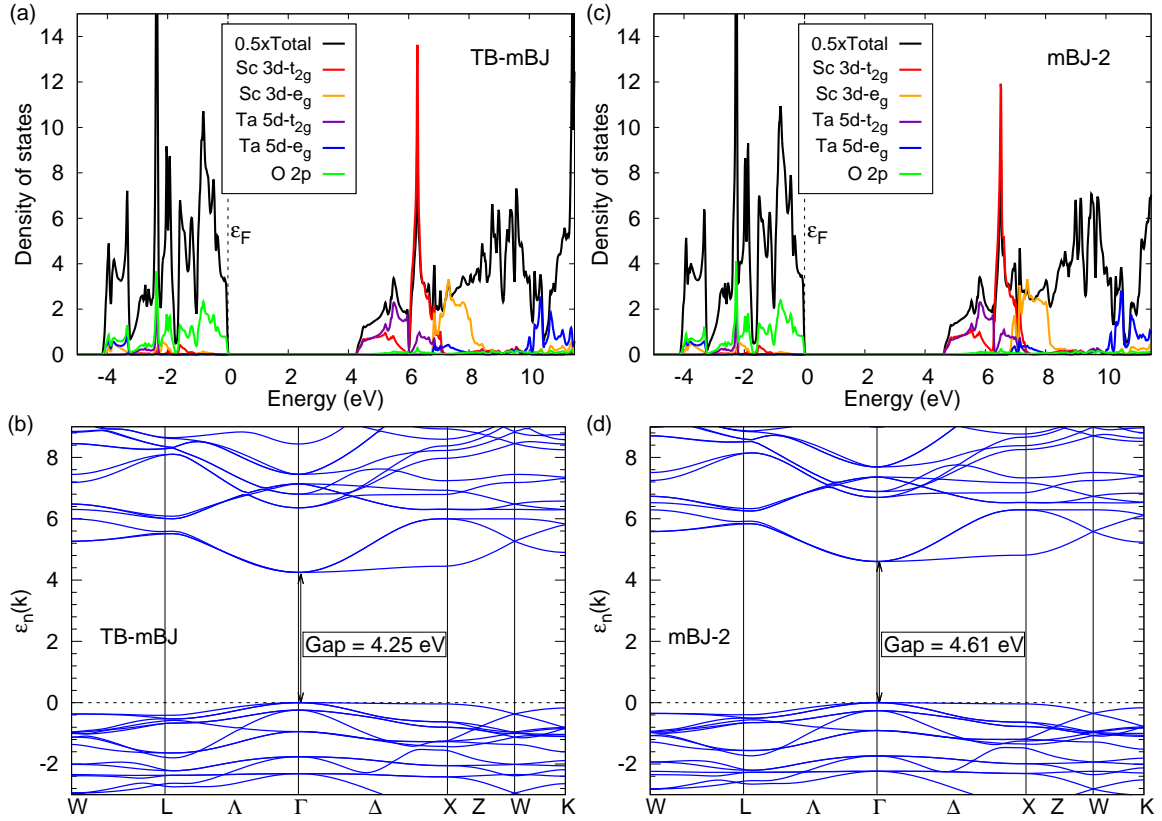


FIG. 4: (Color online.) The total and partial density of states in states/eV-unit cell and states/eV-atom, respectively, and the corresponding bandstructure obtained within (a)-(b) TB-mBJ and (c)-(d) mBJ-2 method.

As observed from the atom- and orbital-resolved DOS, the conduction band edge states have dominant contributions from the Ta- t_{2g} states with small contributions from Sc- t_{2g} states. This is somewhat different from A_2 YTaO₆ DPOs [5] despite similar electronegativity of Y (1.22) and Sc (1.36). In comparison, the electronegativity of Ta is 1.50. The primary reason for this difference is the relatively small energetic overlap between the Y- $4d$ and O- $2p$ states as compared to Sc- $3d$ and O- $2p$ states. Strong covalency effects between Sc-O and Ta-O are also noted. The dominant Ta- t_{2g} and Ta- e_g contributions are found at ~ 4.5 eV and ~ 10 eV, respectively, implying a crystal field splitting of approximately 5.5 eV. On the other hand, the crystal field splitting for Sc- d states is merely ~ 2.2 eV — a consequence of relative electronegativity difference and M-O distances. The relative hybridization between Sc-O is found to be quite

TABLE II: Electronic bandgap obtained within different DFT approximations.

Method	Gap (eV)	Remarks
Experimental	4.66	UV-Vis spectroscopy
PBE-GGA	3.12	
TB-mBJ	4.25	“Option 0” in WIEN2k, defined in Ref. [20].
mBJ-1	4.36	modified mBJ parameters suitable for perovskite oxides; “Option 1” in WIEN2k, defined in Ref. [21].
mBJ-2	4.61	modified mBJ parameters suitable for large bandgap materials; “Option 2” in WIEN2k, defined in Ref. [21].
mBJ-3	5.48	modified mBJ parameters suitable for halide perovskites “Option 4” in WIEN2k, defined in Ref. [22].

smaller than Ta-O as evidenced by the M-*d* DOS in the valence band region. Therefore, an appropriate description of the electronic structure is (large) mixing of Sc-3*d* states with the strongly hybridized Ta-O anti-bonding states.

As shown in Fig. 3(b), the electronic bandstructure within GGA has a direct gap of ~ 3.1 eV, which is much smaller than the gap estimated from the analysis of the absorption data obtain through UV-Vis reflectance spectroscopy. This discrepancy between the theoretical and experimental estimates is a well-known issue within DFT. A computationally efficient way to address this discrepancy is to employ the Tran-Blaha modified-Becke-Johnson (TB-mBJ) exchange-correlation potential [20].

Inclusion of such correction leads to a remarkable improvement in the comparison between the measured and the calculated electronic gap, as shown in Fig. 4(a) & (b). The electronic bandgap within TB-mBJ is approximately 4.25 eV, much closer to the experimental value (only $\sim 7\%$ smaller). Other aspects of the electronic properties only undergo quantitative changes. The conduction band edge has relatively large contribution from Sc-*d* orbitals, implying further enhancement of covalency effects. This is accompanied by reduction of the effective crystal field splitting for the Sc-*d* states to $\gtrsim 1$ eV. For Ta-*d* states in comparison, the crystal field splitting undergoes only marginal change. The bandwidth of the *d* states, for both Sc and Ta, is slightly reduced. It is important to note that these corrections are not a rigid shift of all the conduction band states (“scissors” operation), and, therefore, may significantly influence the optical properties. In comparison to GGA, a simplified view of the application of the orbital-dependent corrections introduced by the mBJ potential could be a band-dependent scissors operation like shifts [31].

Despite its successes, TB-mBJ potential is known to underestimate the gap in many cases [21]. Different parametrizations of the mBJ potential have, therefore, been suggested which are specifically catered to perovskite oxides [21], halide perovskites [22], and large bandgap materials [21]. To further improve the degree of comparison between calculated and measured gap, we first tried the mBJ potential adapted for perovskite oxides (labeled mBJ-1). The resulting bandgap is found to be approximately 4.36 eV. While the situation is improved as compared to TB-mBJ, surprisingly it is still $\sim 4.5\%$ smaller. On the other hand, the version adapted for perovskite halides (labeled mBJ-3), leads to an overestimation presumably due to large electronegativity differences between ligand species (oxygen vs halides). The resulting bandgap is found to be ~ 5.5 eV. An excellent agreement is, however, found for the mBJ potential adapted for large bandgap insulators (labeled mBJ-2). These results are summarized in Table II for brevity, with details related to their implementation in WIEN2k.

The bandgap within mBJ-2 is found to be 4.61 eV which is in excellent agreement with the experimental estimate of 4.66 eV. In terms of the electronic properties, as shown in Fig. 4(c) and (d), DOS and bandstructures are qualitatively similar to TB-mBJ and shows only small quantitative changes. In view of this, to study the optical properties, we consider only the mBJ-2 case.

D. Optical properties

Finite-frequency optical response of materials is captured through their complex dielectric function $\varepsilon_{\mu\nu}(\omega)$ ($\mu, \nu = x, y, z$). For structures with cubic symmetry, only one component of $\varepsilon_{\mu\nu}$ is independent as $\varepsilon_{xx} = \varepsilon_{yy} = \varepsilon_{zz}$. The symmetry relation between different components also holds for other optical response functions.

In the case of Ba₂ScTaO₆, the band edge region consists of multiple excitons (see Sec. III B) which have not been taken into account in the DFT calculations. However, away for the band edge, accurate predictions can be obtained using the mBJ-2 corrections to DFT.

The dielectric function for Ba₂ScTaO₆ for the mBJ-2 method is shown in Fig. 5(a)-(b). The onset of the optical

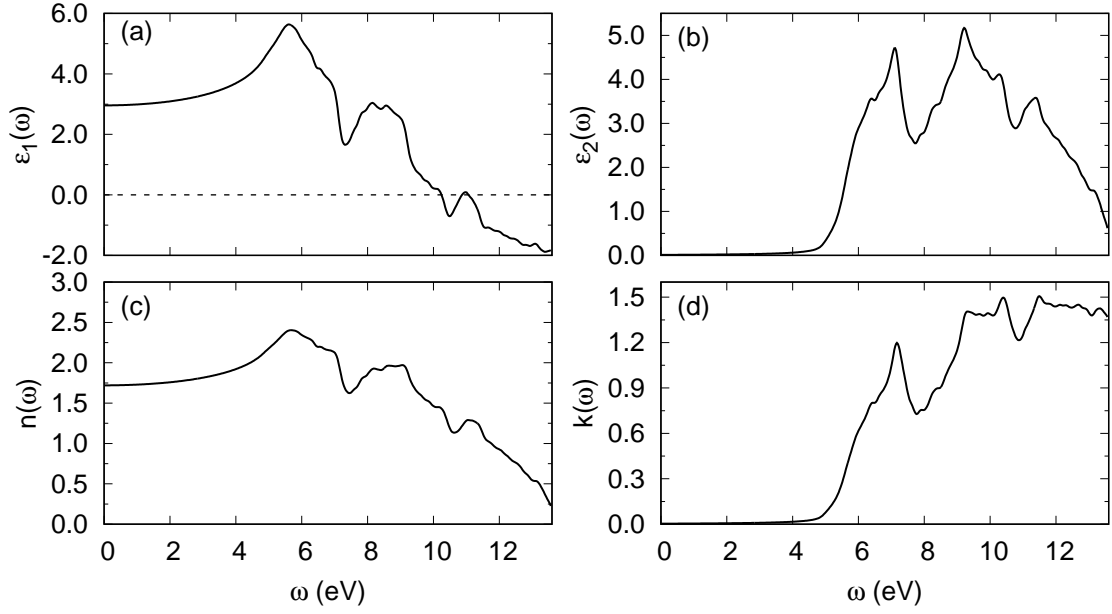


FIG. 5: The (a) real $[\varepsilon_1(\omega)]$ and the (b) imaginary $[\varepsilon_2(\omega)]$ parts of the dielectric function. The (c) real $[n(\omega)]$ and the (d) imaginary $[k(\omega)]$ parts of the refractive index.

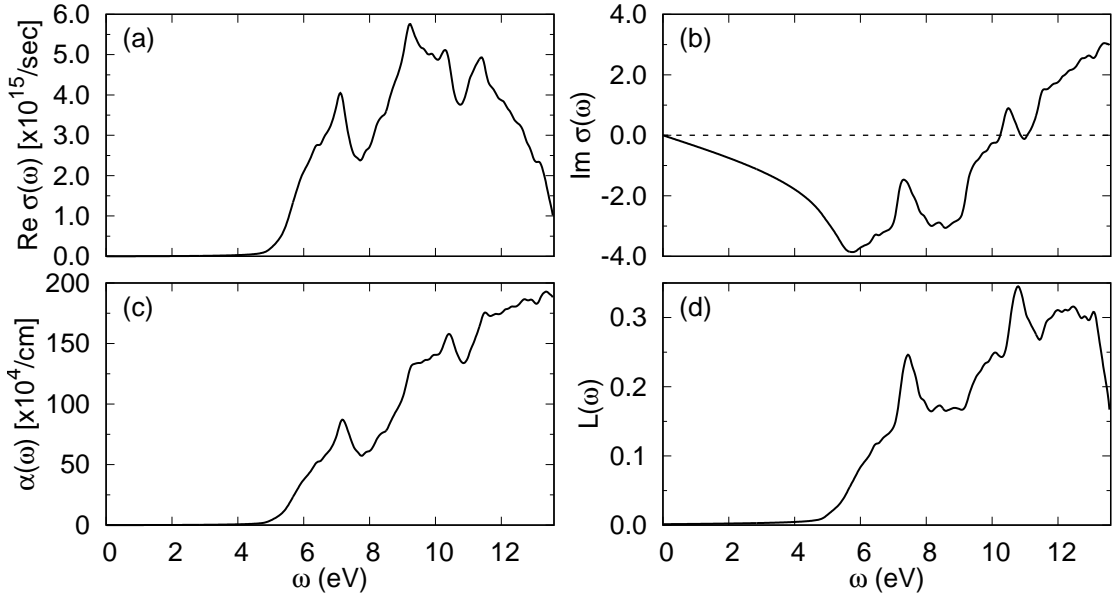


FIG. 6: The (a) real and the (b) imaginary parts of the optical conductivity $\sigma(\omega)$, and the (c) absorption coefficient, and the (d) loss function.

response ε_2 is at a finite frequency, at ~ 4.6 eV, due to the finite electronic bandgap. The peaks in $\varepsilon_2(\omega)$ correspond to optical transitions from states in the valence band to states in the conduction band and are proportional to the joint DOS between the initial and final states involved in such transitions. In general, the optical selection rules dictate if such transitions are allowed. In the present case, as also for most insulating DPOs, the valence band and conduction band states close to the Fermi energy are dominantly of O-2p and M-d characters. As a result, the selection rules are trivially satisfied. Indeed, the transitions between the O-2p states in the valence band and M-d states at the conduction band edge lead to the optical transitions in the entire energy range studied. For example, the features below ~ 6.5 eV can be understood as transitions from the valence band region to the conduction band edge (Ta- t_{2g} states). Similarly, prominent peaks in ε_2 at ~ 7 eV and ~ 11.5 eV arise due to transitions from valence band edge to the Sc- t_{2g} states and transitions from valence band edge to Ta- e_g states, respectively.

The frequency-dependence of the real and imaginary parts of the refractive index closely follows the complex dielectric function, as shown in Fig. 5(c)-(d). They, respectively, correspond to the dispersion and absorption of light passing through the medium. The refraction coefficient peaks at the photon energy of 5.5 eV approximately and reaches a maximum value of ~ 2.4 . The static refractive index, $n(\omega = 0)$, is obtained from the static limit of the real part of the dielectric function: $n = \sqrt{\varepsilon_1(\omega \rightarrow 0)}$, and is found to be 1.72.

The complex optical conductivity $\sigma(\omega) = i\omega\varepsilon(\omega)/4\pi$ is shown in Fig. 6(a)-(b). The low-energy peaks in the real part of the optical conductivity exhibit characteristics similar to the dielectric function $\varepsilon_2(\omega)$, with the prominent peaks at ~ 7 eV, ~ 9.3 eV, ~ 10 eV and ~ 11.5 eV. The dispersive part of the dielectric function, $\varepsilon_1(\omega)$ governs the imaginary part of the optical conductivity. It is negative for small values of photon energy and crosses zero around 10 eV. The zero-crossing energy is consistent with the that of $\varepsilon_1(\omega)$, as expected.

As shown in Fig. 6(c), the absorption edge lies at ~ 4.6 eV and increases with increasing photon energy. The finite value of the absorption edge is due to the bandgap. The peaks around the energies 7 eV and above arise due to inter-band transitions, as discussed earlier.

The Loss function, $L(\omega)$, corresponds to the electron energy loss spectroscopy (EELS) which captures both non-scattering and elastic scattering processes. It is connected to the energy loss of the electrons as they traverse through the medium and lose energy. Typically, the mixing of single electron excitations with the collective excitations (plasmons) gives rise to energy loss of the electrons up to 50 eV.

The loss function for $\text{Ba}_2\text{ScTaO}_6$ is shown in Fig. 6(d) and qualitatively follows the imaginary part of the dielectric function $\varepsilon_2(\omega)$. There are two prominent peaks, lying at ~ 7 eV and ~ 10.6 eV. The first (low-energy) peak at ~ 7 eV, originates from inter-band transitions between O-2p to M-d states as discussed earlier, while the latter originates from transitions between semi-core states to conduction band edge.

IV. CONCLUSIONS

To summarize, we have experimentally determined the crystal structure, optical and electronic gap of $\text{Ba}_2\text{ScTaO}_6$ and theoretically investigated its electronic and optical properties. Contrary to the earlier prediction based on GGA, the experimental electronic gap of $\text{Ba}_2\text{ScTaO}_6$ is found to be ~ 4.7 eV, which is similar to other Ta-based d^0 -DPOs. An excellent quantitative agreement between experiment and DFT is obtained upon considering also the adapted mBJ potential suggested for large gap insulators. Other mBJ potential considered in this study, although better than GGA, still performs rather poorly, including the one adapted for perovskite oxides.

An important finding of this study is the presence of multiple low-energy exciton modes in $\text{Ba}_2\text{ScTaO}_6$ which extend well into the visible range of the electromagnetic spectrum, thus affecting its optical response. This may have remarkable consequences for other predicted large bandgap DPOs, especially Ta-based DPOs. Such materials are considered potential functional materials and may find use as microwave dielectric resonators, interference filters, buffer materials as well as photocatalysts. However, to ascertain their utility, the electronic and optical properties should perhaps be revisited in the light of our findings.

Acknowledgements

AKH and SK thank Dr. V. Srihari for the SXRD experimental support at BL-11, RRCAT, Indore. RR and UD thank Ulrike Nitzsche for technical assistance with the computational resources in IFW Dresden. RR also thanks Dhiraj Kushvaha for technical assistance.

Competing Interests

The authors declare that they have no known competing financial interests or personal relationships that could have appeared to influence the work reported in this paper.

Author contributions

AKH and SK carried out the synthesis and characterization of the material. AKH and RR carried out the DFT calculations. UD carried out the exciton analysis with help from RR. UD and RR prepared the manuscript with contributions from all authors. AKH and RR were responsible for project planning.

Data availability

The raw/processed data required to reproduce these findings cannot be shared at this time as the data also forms part of an ongoing study.

-
- [1] A. W. Sleight, R. Ward, Compounds of heptavalent rhenium with the perovskite structure, *Journal of the American Chemical Society* 83 (5) (1961) 1088–1090.
- [2] F. K. Patterson, C. W. Moeller, R. Ward, Magnetic oxides of molybdenum (V) and tungsten (V) with the ordered perovskite structure, *Inorganic Chemistry* 2 (1) (1963) 196–198.
- [3] S. Vasala, M. Karppinen, $A_2B'B''O_6$ perovskites: A review, *Progress in Solid State Chemistry* 43 (1-2) (2015) 1–36. doi:10.1016/j.progsolidstchem.2014.08.001. URL <https://doi.org/10.1016/j.progsolidstchem.2014.08.001>
- [4] T. Saha-Dasgupta, Double perovskites with 3d and 4d/5d transition metals: compounds with promises, *Materials Research Express* 7 (1) (2020) 014003. doi:10.1088/2053-1591/ab6293. URL <https://doi.org/10.1088/2053-1591/ab6293>
- [5] H. W. Eng, P. W. Barnes, B. M. Auer, P. M. Woodward, Investigations of the electronic structure of d^0 transition metal oxides belonging to the perovskite family, *Journal of Solid State Chemistry* 175 (1) (2003) 94–109. doi:10.1016/s0022-4596(03)00289-5. URL [https://doi.org/10.1016/s0022-4596\(03\)00289-5](https://doi.org/10.1016/s0022-4596(03)00289-5)
- [6] R. Ray, A. Himanshu, P. Sen, U. Kumar, M. Richter, T. Sinha, Effects of octahedral tilting on the electronic structure and optical properties of d^0 double perovskites A_2ScSbO_6 ($A=Sr, Ca$), *Journal of Alloys and Compounds* 705 (2017) 497–506. doi:10.1016/j.jallcom.2017.02.080. URL <https://doi.org/10.1016/j.jallcom.2017.02.080>
- [7] W.-J. Yin, B. Weng, J. Ge, Q. Sun, Z. Li, Y. Yan, Oxide perovskites, double perovskites and derivatives for electrocatalysis, photocatalysis, and photovoltaics, *Energy Environ. Sci.* 12 (2019) 442–462. doi:10.1039/C8EE01574K. URL <http://dx.doi.org/10.1039/C8EE01574K>
- [8] R. Ray, A. K. Himanshu, G. K. Mandal, U. Kumar, S. N. Jha, N. Patra, D. Bhattacharya, A. B. Shinde, M. Richter, P. S. R. Krishna, Revised crystal structure and electronic properties of high dielectric $ba(fe1/2nb1/2)o_3$ ceramics, *Journal of Applied Physics* 130 (21) (2021) 214101. doi:10.1063/5.0068825. URL <https://doi.org/10.1063/5.0068825>
- [9] W. Travis, E. N. K. Glover, H. Bronstein, D. O. Scanlon, R. G. Palgrave, On the application of the tolerance factor to inorganic and hybrid halide perovskites: a revised system, *Chem. Sci.* 7 (2016) 4548–4556. doi:10.1039/C5SC04845A. URL <http://dx.doi.org/10.1039/C5SC04845A>
- [10] K. K. Pandey, H. K. Poswal, A. K. Mishra, A. Dwivedi, R. Vsanthi, N. Garg, S. M. Sharma, Energy-dispersive x-ray diffraction beamline at Indus-2 synchrotron source, *Pramana* 80 (4) (2013) 607–619. doi:10.1007/s12043-012-0493-0. URL <https://doi.org/10.1007/s12043-012-0493-0>
- [11] J. Rodríguez-Carvajal, Recent advances in magnetic structure determination by neutron powder diffraction, *Physica B: Condensed Matter* 192 (1-2) (1993) 55–69.
- [12] E. A. Davis, N. F. Mott, Conduction in non-crystalline systems v. conductivity, optical absorption and photoconductivity in amorphous semiconductors, *Philosophical Magazine* 22 (179) (1970) 0903–0922. doi:10.1080/14786437008221061. URL <https://doi.org/10.1080/14786437008221061>
- [13] D. G. Barton, M. Shtein, R. D. Wilson, S. L. Soled, E. Iglesia, Structure and electronic properties of solid acids based on tungsten oxide nanostructures, *The Journal of Physical Chemistry B* 103 (4) (1999) 630–640. doi:10.1021/jp983555d. URL <https://doi.org/10.1021/jp983555d>
- [14] R. J. Elliott, Intensity of optical absorption by excitons, *Phys. Rev.* 108 (1957) 1384–1389. doi:10.1103/PhysRev.108.1384. URL <https://link.aps.org/doi/10.1103/PhysRev.108.1384>
- [15] T. Wang, B. Daiber, J. M. Frost, S. A. Mann, E. C. Garnett, A. Walsh, B. Ehrler, Indirect to direct bandgap transition in methylammonium lead halide perovskite, *Energy Environ. Sci.* 10 (2017) 509–515. doi:10.1039/C6EE03474H. URL <http://dx.doi.org/10.1039/C6EE03474H>
- [16] P. Blaha, K. Schwarz, G. K. H. Madsen, D. Kvasnicka, J. Luitz, R. Laskowski, F. Tran, L. D. Marks, WIEN2k, an augmented plane wave + local orbitals program for calculating crystal properties, (Karlheinz Schwarz, Techn. Universität Wien, Austria) (2018).
- [17] P. Blaha, K. Schwarz, F. Tran, R. Laskowski, G. K. H. Madsen, L. D. Marks, WIEN2k: An APW+lo program for calculating the properties of solids, *The Journal of Chemical Physics* 152 (7) (2020) 074101. doi:10.1063/1.5143061. URL <https://doi.org/10.1063/1.5143061>
- [18] J. P. Perdew, K. Burke, M. Ernzerhof, Generalized gradient approximation made simple, *Physical Review Letters* 77 (18) (1996) 3865–3868. doi:10.1103/physrevlett.77.3865. URL <https://doi.org/10.1103/physrevlett.77.3865>

- [19] E. J. Baerends, O. V. Gritsenko, R. van Meer, **The kohn–sham gap, the fundamental gap and the optical gap: the physical meaning of occupied and virtual kohn–sham orbital energies**, *Physical Chemistry Chemical Physics* 15 (39) (2013) 16408. doi:10.1039/c3cp52547c. URL <https://doi.org/10.1039/c3cp52547c>
- [20] F. Tran, P. Blaha, **Accurate band gaps of semiconductors and insulators with a semilocal exchange–correlation potential**, *Phys. Rev. Lett.* 102 (2009) 226401. doi:10.1103/PhysRevLett.102.226401. URL <https://link.aps.org/doi/10.1103/PhysRevLett.102.226401>
- [21] D. Koller, F. Tran, P. Blaha, **Improving the modified Becke–Johnson exchange potential**, *Phys. Rev. B* 85 (2012) 155109. doi:10.1103/PhysRevB.85.155109. URL <https://link.aps.org/doi/10.1103/PhysRevB.85.155109>
- [22] R. A. Jishi, O. B. Ta, A. A. Sharif, **Modeling of lead halide perovskites for photovoltaic applications**, *The Journal of Physical Chemistry C* 118 (49) (2014) 28344–28349. doi:10.1021/jp5050145. URL <https://doi.org/10.1021/jp5050145>
- [23] C. Ambrosch-Draxl, J. Sofo, **Linear optical properties of solids within the full-potential linearized augmented planewave method**, *Computer Physics Communications* 175 (1) (2006) 1–14. doi:10.1016/j.cpc.2006.03.005.
- [24] **Ba2tasco6 (ba2sctao6) crystal structure: Datasheet from “pauling file multinaries edition – 2012” in springer materials** (https://materials.springer.com/isp/crystallographic/docs/sd_1701174), copyright 2016 Springer-Verlag Berlin Heidelberg & Material Phases Data System (MPDS), Switzerland & National Institute for Materials Science (NIMS), Japan. URL https://materials.springer.com/isp/crystallographic/docs/sd_1701174
- [25] V. Filipev, E. Fesenko, **Symmetry and lattice parameters of some composite perovskites**, *SOVIET PHYSICS CRYSTALLOGRAPHY*, USSR 10 (5) (1966) 532.
- [26] M. W. Lufaso, P. W. Barnes, P. M. Woodward, **Structure prediction of ordered and disordered multiple octahedral cation perovskites using SPuDS**, *Acta Crystallographica Section B Structural Science* 62 (3) (2006) 397–410. doi:10.1107/S010876810600262x. URL <https://doi.org/10.1107/S010876810600262x>
- [27] P. D. C. King, T. D. Veal, F. Fuchs, Ch. Y. Wang, D. J. Payne, A. Bourlange, H. Zhang, G. R. Bell, V. Cimalla, O. Ambacher, R. G. Egdell, F. Bechstedt, C. F. McConville, **Band gap, electronic structure, and surface electron accumulation of cubic and rhombohedral In₂O₃**, *Phys. Rev. B* 79 (2009), 205211. doi:10.1103/PhysRevB.79.205211. URL <https://doi.org/10.1103/PhysRevB.79.205211>
- [28] L. Chiodo, J. M. García-Lastra, A. Iacomino, S. Ossicini, J. Zhao, H. Petek, A. Rubio, **Self-energy and excitonic effects in the electronic and optical properties of TiO₂ crystalline phases**, *Phys. Rev. B* 82 (2010), 045207. doi:10.1103/PhysRevB.82.045207. URL <https://doi.org/10.1103/PhysRevB.82.045207>
- [29] S. John, C. Soukoulis, M. H. Cohen, E. N. Economou, **Theory of electron band tails and the urbach optical-absorption edge**, *Phys. Rev. Lett.* 57 (1986) 1777–1780. doi:10.1103/PhysRevLett.57.1777. URL <https://link.aps.org/doi/10.1103/PhysRevLett.57.1777>
- [30] J. Viljanen, **A unified pervasive linebroadening function for quantum wells in light emitting diodes**, *Applied Sciences* 10 (11). doi:10.3390/app10113774. URL <https://www.mdpi.com/2076-3417/10/11/3774>
- [31] B. Sadhukhan, Y. Zhang, R. Ray, J. van den Brink, **First-principles calculation of shift current in chalcopyrite semiconductor ZnSnP₂**, *Phys. Rev. Materials* 4 (2020) 064602. doi:10.1103/PhysRevMaterials.4.064602. URL <https://link.aps.org/doi/10.1103/PhysRevMaterials.4.064602>